WO_3 Nanoflakes for Enhanced Photoelectrochemical Conversion

Wenjie Li,[†,§] Peimei Da,[†,§] Yueyu Zhang,[‡] Yongcheng Wang,[†] Xuan Lin,[†] Xingao Gong,[‡] and Gengfeng Zheng[*,†]

[†]Laboratory of Advanced Materials, Department of Chemistry and [‡]Key Laboratory of Computational Physical Sciences, State Key Laboratory of Surface Physics, and Department of Physics, Fudan University, Shanghai, 200433, China. [§]W.L. and P.D. contributed equally to this work.

ABSTRACT We developed a postgrowth modification method of two-dimensional WO_3 nanoflakes by a simultaneous solution etching and reducing process in a weakly acidic condition. The obtained dual etched and reduced WO_3 nanoflakes have a much rougher surface, in which oxygen vacancies are created during the simultaneous etching/reducing process for optimized photoelectrochemical performance. The obtained photoanodes show an enhanced photocurrent density of ~1.10 mA/cm^2 at 1.0 V *vs* Ag/AgCl (~1.23 V *vs* reversible hydrogen electrode), compared to 0.62 mA/cm^2 of pristine WO_3 nanoflakes. The electrochemical impedance spectroscopy measurement and the density functional theory calculation demonstrate that this improved performance of dual etched and reduced WO_3 nanoflakes is attributed to the increase of charge carrier density as a result of the synergetic effect of etching and reducing.

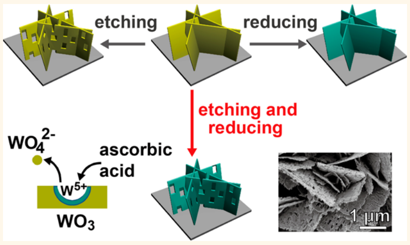

KEYWORDS: photoelectrochemical · WO_3 · nanoflakes · etching · reducing · oxygen vacancy

Nanostructured semiconductor transition metal oxide materials, such as TiO_2,[1−3] Fe_2O_3,[4−6] and WO_3,[7,8] have been among the research foci for solar-energy-driven photoelectrochemical (PEC) conversion. Central to the success of this field includes the rational design/synthesis of semiconductor photoelectrodes with sufficient light absorption, efficient charge separation, and fast transport.[9−11] WO_3 is regarded as an attractive candidate for a photoanode, as it exhibits approximately 12% of solar spectrum absorption (E_g = 2.5−2.8 eV), a moderate hole diffusion length (~150 nm) compared with α-Fe_2O_3 (2−4 nm), and inherently good electron transport properties (~12 cm^2 V^{-1} s^{-1}) compared with TiO_2 (0.3 cm^2 V^{-1} s^{-1}).[12] Nonetheless, WO_3 still suffers from its sluggish kinetics of holes, slow charge transfer at the semiconductor/electrolyte interface, and rapid electron−hole recombination.[12] Substantial efforts have been focused on improving the photocatalytic activity of WO_3, including selective doping of semiconductors,[13] construction of hybrid structures,[8,14] and synthesis of nanostructured WO_3, such as nanowires,[15] nanoflakes,[16] nanobowls,[17] and nanoparticles.[18] In particular, the material morphology control by chemical etching has been demonstrated as a promising means to increase surface area, leading to faster charge transfer and lower overpotential for oxygen and hydrogen evolution.[15] For instance, a hydrothermal chemical method with simultaneous etching/regrowing/doping for post-treatment of TiO_2 nanowires was reported recently.[19] The obtained W-doped TiO_2 core−shell nanowires with an amorphous shell have a much improved photoactivity. Pan *et al.* reported a large-scale synthesis of urchin-like mesoporous TiO_2 hollow spheres by targeted etching, with enhanced PEC properties.[20] The effect of chemical etching has also been demonstrated on other materials such as GaN[21] and CuO.[22]

On the other hand, oxygen vacancies serve as shallow donors for metal oxides such as TiO_2, WO_3, and α-Fe_2O_3, thus improving electrical conductivity and facilitating charge transfer between the metal oxide and the electrolyte.[23] The photoactivity enhancement of hydrogen-annealed WO_3 has been shown as a result of increased donor density by introducing a moderate amount of oxygen vacancies and forming substoichiometric WO_{3-x}.[24] Wang *et al.* reported the narrowing of the SnO_2 band gap by hydrothermal Sn^{2+} self-doping, during which the accompanying oxygen vacancies result in the shifting of Fermi energy, thus

* Address correspondence to gfzheng@fudan.edu.cn.

Received for review September 22, 2014 and accepted October 27, 2014.

10.1021/nn5053684

improving interfacial charge transfer and overall PEC performance.[25] These treatments for creating oxygen vacancies typically require high annealing temperatures (*e.g.*, 300−500 °C) or hydrothermal conditions, as the removal of oxygen atoms from the lattice consumes substantial energy. Solution treatment under an ambient or relatively low temperature condition, however, is much less effective, as the solution reaction mainly takes place at the oxide surface, while the majority of the bulk structures remain unchanged. Very recently, a solution reduction method using $NaBH_4$ was demonstrated for effectively increasing oxygen vacancies in TiO_2 and Co_3O_4,[26,27] while this method is inadequate for treatment of WO_3, due to its instability in basic or neutral pH conditions.

Herein, we report a postgrowth, dual etching, and reducing method of pregrown WO_3 nanoflakes in a weakly acidic condition, which allows for controlled introduction of oxygen vacancies (*i.e.*, reducing W^{6+} to W^{5+}) at mild solution conditions and enhanced PEC performance. After this dual etching and reducing step, WO_3 nanoflakes with a much rougher surface are obtained, suggesting increased interfacial area for solution reduction and electrochemical reaction. In addition, oxygen vacancies are simultaneously formed during this etching/reducing process for enhanced PEC activity. A high photocurrent density of 1.10 mA/cm^2 at 1.0 V *vs* Ag/AgCl (1.23 V *vs* reversible hydrogen electrode, RHE) is obtained, compared to 0.62 mA/cm^2 of pristine WO_3 nanoflakes. The Mott−Schottky plots and the density functional theory (DFT) simulation illustrate that the etching process decreases the band edge of TiO_2 and is beneficial to the charge transfer, while the effective oxygen vacancies increase the charge carrier density of WO_3 nanoflakes. These two synergistic effects contribute to the finally enhanced PEC performance of the dual etched/reduced WO_3 nanoflakes.

RESULTS AND DISCUSSION

The WO_3 nanoflake arrays were synthesized on fluorine-doped tin oxide (FTO) glass substrates by a modified hydrothermal method reported previously (Methods).[15] After the hydrothermal reaction and subsequent annealing in air, the FTO glass substrate was covered with a thin layer of light yellow, uniform film. Scanning electron microscopy (SEM) images show that this film is composed of vertically aligned WO_3 nanoflakes (Figure 1a,b). The thickness of the nanoflakes is typically 20−30 nm, with a height of less than 2 μm. High-resolution transmission electron microscopy (HRTEM) images further reveal that the nanoflakes have a single-crystalline structure (Figure 1c), which is clearly displayed by the corresponding fast Fourier transform (FFT) pattern (Figure 1c, inset). Lattice fringes of 0.385 and 0.365 nm are clearly observed, corresponding to the *d*-spacing values of the (200) and (002) planes of monoclinic WO_3, respectively.[28] The annealed WO_3 nanoflakes were transferred into a weakly acidic solution containing poly(vinyl pyrrolidone) (PVP) and ascorbic acid (pH ∼4.5) to obtain the dual etched/reduced WO_3 nanoflakes (Methods). After the reaction, a slightly blue color change is observed on the treated WO_3 nanoflake samples, suggesting the modification of the light absorption profile. The nanoflake surface becomes much rougher with porous morphologies (Figure 1d,e). TEM image exhibits that the dual etched/reduced nanoflakes have a porous surface morphology with holes of various sizes (Figure 1f). No impurities are shown by the energy-dispersive X-ray spectroscopy (EDX, Supporting Information Figure S1). For comparison, when ascorbic acid is absent from the reaction solution, a similar porous nanoflake morphology is also obtained (Figure S2a), suggesting that PVP provides an etching effect for the obtained nanoflakes (designated as the etched WO_3). The selective etching of the WO_3 nanoflakes can be attributed to the small difference of crystal structure and surface energy on the WO_3 nanoflake surface.[29] On the other hand, if the reaction solution contains only ascorbic acid but without PVP, the resulting nanoflakes (designated as the reduced WO_3) present a negligible difference in the surface morphology compared to the pristine WO_3 nanoflakes (Figure S2b), suggesting the reducing effect of ascorbic acid.

The crystal structures and the possible phase change of the dual etched/reduced WO_3 nanoflakes are examined by X-ray diffraction (XRD, Figure S3a). The pristine WO_3 nanoflakes can be well indexed into a monoclinic structure (JCPDS No. 43-1035). The dual etched/reduced WO_3 nanoflakes show no observable shifts of all characteristic diffraction peaks compared to pristine WO_3 nanoflakes, indicating that the main crystal structure is preserved during the treatment. To further elucidate the chemical states of dual etched/reduced WO_3 nanoflakes, we used X-ray photoelectron spectroscopy (XPS) for the pristine and the dual etched/reduced WO_3 nanoflakes. These two types of WO_3 nanoflakes have similar normalized high-resolution O 1s spectra (Figure S3b), indicating that the coordination polyhedron of oxygen around each W is not much affected.[30] In addition, the absence of the hydroxyl (O−H) peak or broader shoulder around 532 eV indicates no formation of tungsten bronze (H_xWO_3), which is also blue in color.[31] The normalized XPS W 4f spectra of pristine WO_3 nanoflakes (Figure S3c, black curve) have two peaks, corresponding to the characteristic W $4f_{5/2}$ and W $4f_{7/2}$ peaks for WO_3.[32] The W 4f XPS peak of the dual etched/reduced WO_3 (red curves in Figure S3c,d) can be deconvoluted into two pairs of peaks, corresponding to the typical binding energies of two W oxidation states, W^{6+} (centered at 37.5 and 35.6 eV) and W^{5+} (centered at 36.4 and 34.4 eV) (Figure S3d).[32] The data suggest that a substantial amount of W^{6+} is reduced to W^{5+} (or forming oxygen vacancies) in the dual etched/reduced WO_3 nanoflakes.

To evaluate the PEC conversion performance of the dual etched/reduced WO_3 nanoflakes, the pristine

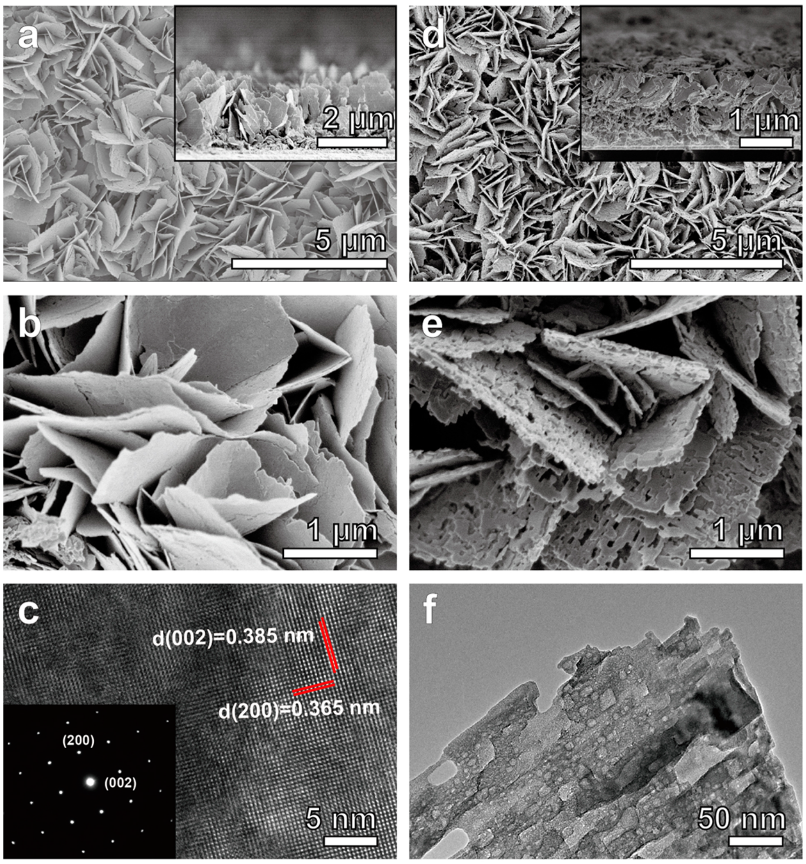

Figure 1. (a,b) SEM and (c) HRTEM images of pristine WO_3 nanoflakes. (d,e) SEM and (f) HRTEM images of the dual etched/reduced WO_3 nanoflakes. Insets in (a,d): SEM images of the cross sections of films. Inset in (c): diffraction pattern.

WO_3 nanoflakes, etched WO_3 nanoflakes, reduced WO_3 nanoflakes, and the dual etched/reduced WO_3 nanoflakes were fabricated as photoanodes with an exposed surface area of ~1 cm^2 and measured under simulated solar light illumination (Methods). The photocurrent density of the pristine WO_3 nanoflakes is 0.62 mA/cm^2 at 1.0 V *vs* Ag/AgCl (~1.23 V *vs* RHE) (Figure 2a, black curve), comparable to previous reports.[15] The etched (green curve) or reduced WO_3 nanoflakes (blue curve) exhibit photocurrent densities of ~0.75 and ~0.85 mA/cm^2, indicating the etching and reducing effects on the photoactivity of WO_3, respectively. Remarkably, the dual etched/reduced WO_3 nanoflakes (red curve) reach ~1.10 mA/cm^2 at 1.0 V *vs* Ag/AgCl, which is the highest among the four types of samples. For comparison, WO_3 nanoflakes that were sequentially etched, followed by the reducing process (designated as the two-step treatment), were measured under similar conditions (Figure 2b). Notably, the magnitude of the photocurrent density increase by this two-step process is similar to that of the etching-only or reducing-only samples but much less than that of the one-step simultaneous etching/reducing approach, thus clearly indicating the synergetic effect of the simultaneous etching/reducing method. During the simultaneous etching/reducing process, more crystal lattices are exposed and subsequently etched, contributing substantially to the increase of oxygen vacancies. However, in the case of the two-step process (*i.e.*, first etched then reduced), the surface area of the pre-etched nanoflakes remains almost unchanged during the reduction step, which is much less effective for the formation of oxygen vacancies.

To illustrate the origin of the PEC enhancement, the UV−vis absorption spectra of the dual etched/reduced WO_3 nanoflakes were measured, which show a slight red shift compared to the pristine ones (Figure 2c). The optical band gaps (E_g) are further extrapolated using the following equation:[33] $\alpha h\nu = A(h\nu - E_g)^n$, where h is Planck's constant, ν is the frequency of light, A is a constant, and n is equal to 1/2 for an allowed direct transition, such as in WO_3. The calculated E_g values of both samples are consistent with the band gap of monoclinic WO_3 (~2.6 eV),[7] while a slight decrease of the band gap (~0.1 eV) is also observed for the dual etched/reduced WO_3 nanoflakes. Moreover, to evaluate the external quantum efficiency of these four nanoflake samples at different wavelength regions, the incident photo-to-current conversion efficiency (IPCE) measured at 1.0 V *vs* Ag/AgCl is displayed from 320 to 600 nm (Figure 2d). The photocurrent responses of all four samples are mainly located in the wavelength region below 475 nm and decrease to almost zero above 475 nm. The "etched" WO_3 nanoflakes (green

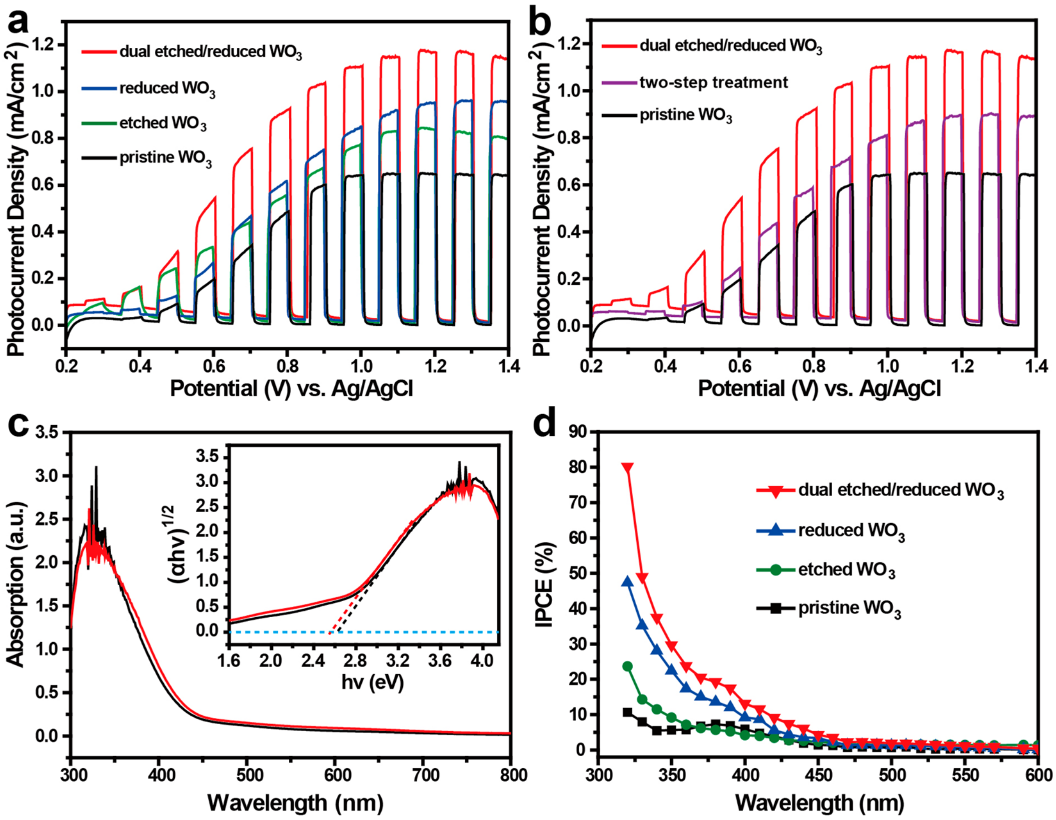

Figure 2. (a) Photocurrent density curves of four types of WO$_3$ nanoflakes. (b) Photocurrent density curves for pristine WO$_3$ nanoflakes, the dual etched/reduced WO$_3$ nanoflakes by one-step growth, and the subsequent two-step etching and reducing of WO$_3$ nanoflakes. (c) UV−vis absorption spectra and the extracted band gap profile of pristine WO$_3$ nanoflakes and the dual etched/reduced WO$_3$ nanoflakes. (d) IPCE spectra of the four types of WO$_3$ nanoflakes measured at 1.0 V *vs* Ag/AgCl.

curve) have a slightly higher IPCE profile than that of pristine WO$_3$ nanoflakes (black curve), indicating that the effect of etching contributes more active PEC reaction sites. On the other hand, an obvious increase of the "reduced" WO$_3$ nanoflakes (blue curve) demonstrates the role of oxygen vacancies for the photoactivity improvement. The dual etched/reduced WO$_3$ nanoflakes (red curve) present the highest IPCE profile, which is over 80% at 320 nm and substantially higher than all the other three samples over 475 nm.

On the basis of the characterization above for the four types of WO$_3$ nanoflakes, a simultaneous etching/reducing mechanism is proposed for the dual etched/reduced WO$_3$ nanoflakes (Figure 3). It has been reported that crystalline WO$_3$ can be etched by potentiostatic anodization to expose active reaction sites.[34] In our weakly acidic solution with pH ∼4.5, a similar etching effect that forms a new surface area and reaction sites is also expected. As more surface area is exposed during the etching process, the ascorbic acid in the solution also simultaneously reduces W^{6+} to W^{5+} and increases the densities of effective oxygen vacancies. Thus, this simultaneous etching and reducing effect resulting from the coexistence of PVP and ascorbic acid provides a better synergetic effect than the "etching-only" and the "reducing-only" processes, resulting in much enhanced photoactivity.

This mechanism is further investigated by electrochemical impedance spectroscopy (EIS) measurements. The Mott−Schottky plots of the pristine, the etched, the reduced, and the dual etched/reduced WO$_3$ nanoflakes are displayed (Figure 4a). All samples show positive slopes as expected for n-type WO$_3$ semiconductors. The flat band potential (E_{fb}) is estimated by extrapolating each Mott−Schottky plot to the *x*-axis to obtain the intercept value. The charge carrier density (N_d) can also be calculated using the following equation:[35]

$$N_d = (2/e\varepsilon_0\varepsilon)[d(1/C^2)/dV]^{-1}$$

For WO$_3$ ($\varepsilon = 20$), the E_{fb} and N_d values are calculated and summarized in Table 1. Compared to the pristine WO$_3$ nanoflakes, the etched WO$_3$ nanoflakes show positive shifts of E_{fb}, suggesting a decrease in the bending of band edges.[35] The flat band shift has a major effect on the increase of the photocurrent for the etched and the dual etched/reduced WO$_3$ nanoflakes. This decrease of band edge bending can be attributed to the increased semiconductor/electrolyte interface, similar to previous reports.[19] However, a decrease of charge carrier density is observed in the etched WO$_3$ nanoflakes. This charge carrier density decrease is due to the increased surface roughness resulting from etching, which worsens the recombination of charge

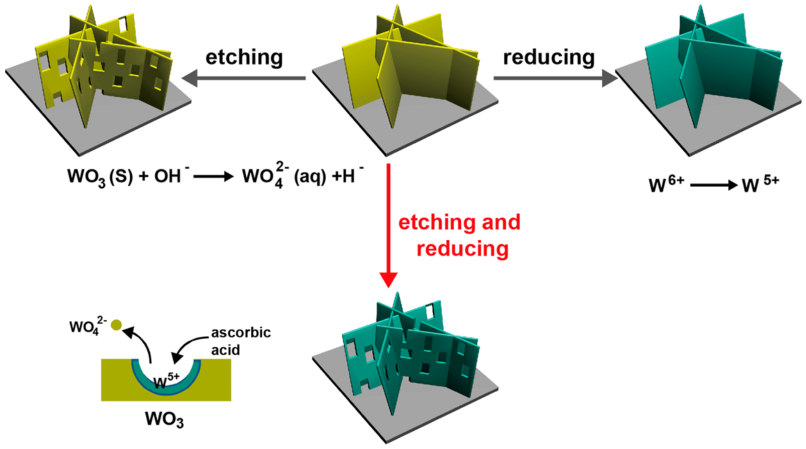

Figure 3. Schematic illustration of the dual etching and reducing mechanism for WO_3 nanoflakes.

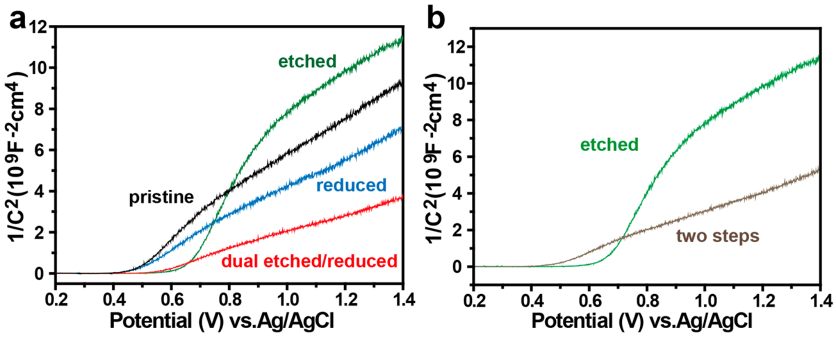

Figure 4. (a) Mott–Schottky plots for the four types of WO_3 nanoflakes. (b) Mott–Schottky plot comparison of the etched WO_3 nanoflakes and the two-step etching and reducing of WO_3 nanoflakes.

TABLE 1. Flat Band Potential (E_{fb}) and Charge Carrier Density (N_d) of WO_3 Nanoflakes (NFs)

sample	E_{fb} (V) *vs* Ag/AgCl	$N_d/10^{20}$ cm^{-3}
pristine WO_3 NF	0.47	5.92
etched WO_3 NF	0.66	2.71
reduced WO_3 NF	0.44	7.63
dual etched/reduced WO_3 NF	0.56	15.1

carriers. On the other hand, both the reduced and dual etched/reduced WO_3 nanoflakes exhibit an increase of charge carrier density, which is attributed to the effective reducing of W^{6+} and increasing of oxygen vacancies in the WO_3 lattice, in good accord with the PEC activities. Moreover, the charge carrier density after the two-step treatment is larger than that of the etched WO_3 nanoflakes yet smaller than that of the dual etched/reduced WO_3 nanoflakes (Figure 4b). This is consistent with photocurrent density measurement, suggesting that the dual etching/reducing treatment is more effective than the two-step treatment.

Density functional theory was then applied to simulate the structural relaxation and electronic structure calculation. In order to understand the rule of the oxygen vacancy on the WO_3 surface, the *ab initio* calculation was carried out to investigate the electronic structure property. O vacancies on the WO_3 (001) surface are studied by performing DFT calculation with the periodic slab models[36] (Methods). A room temperate phase, γ-monoclinic, is used as the unit cell model (Figure 5a). The clean surface is built from cleaving the (001) surface on the O plane from a γ-monoclinic WO_3 supercell with 24 W atoms and 72 O atoms (Figure 5b). The stoichiometric proportion is preserved by removing one-half of the O atoms on the top and bottom O plane. O vacancy is created by removing one O atom on the clean surface (Figure 5c). Formation energy of an oxygen vacancy on the surface is calculated in both O-rich and O-poor conditions, and the results suggest that O vacancies are easier to form in the O-poor condition (Appendix in the Supporting Information). The density of states of the WO_3 unit cell, a clean surface, and the surface with O vacancies are plotted in Figure 5d. The band gap of the unit cell is calculated to be 1.52 eV. As the band gap is often underestimated by the Perdew–Burke–Ernzerhof method,[37] here a scissor operator is applied to shift the gap to 2.20 eV because the O vacancy is a deep donor on the WO_3 surface. From the partial density of states of the unit cell, the valence band maximum (VBM) is mainly occupied by O 2p orbitals and the conduction band minimum (CBM) is mainly composed by the W 5d orbitals. From the difference between the top and the middle panel of Figure 5d, when a (001) surface is cleaved,

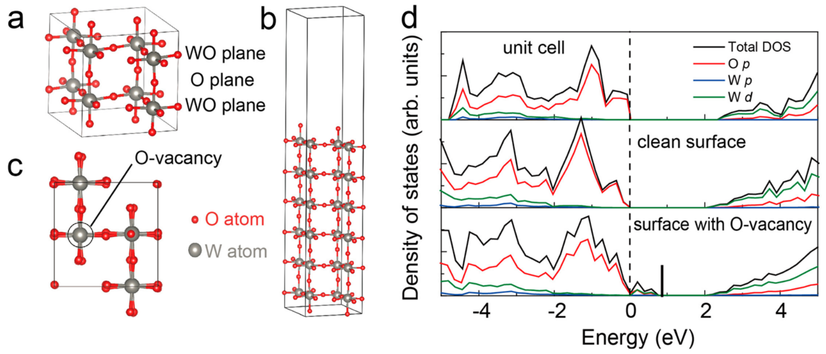

Figure 5. (a) Atomic structure of the monoclinic phase. (b) Clean surface of ($\sqrt{2} \times \sqrt{2}$)*R*45°. (c) Top view of the surface with an oxygen vacancy. (d) Total and partial density of states of the WO_3 unit cell, a clean surface, and a surface with O vacancies. The valence band maximum for pure WO_3 (dashed vertical line) is taken as the reference level. Short black lines in the bottom panel point to the Fermi energy of the doped system.

the band gap is narrowed by 0.28 eV, while the characteristics of CBM and VBM remain similar to those of the bulk system. The narrowing of the band gap can be attributed to the distortion of the surface atoms and charge redistribution near the surface. Some occupied states appear in the gap region with the introduction of O vacancies and narrow the band gap to 1.54 eV. The O vacancy also creates charge carriers to the system. Thus, this simulation suggests that the increasing of charge carrier density and narrowing of band gap lead to the enhancement of photocurrent density of WO_3 slab with O vacancies.

CONCLUSIONS

In summary, we have developed a solution-based, simultaneous etching and reducing method for improving the PEC activity of pregrown WO_3 nanoflakes. The etching effect provides a much increased surface site for the reducing process to take place simultaneously, as well as the subsequent PEC reaction. In the meanwhile, the reducing effect leads to a substantial increase of oxygen vacancies and charge carrier densities. This simultaneous etching and reducing method is convenient and facile and requires only mild solution conditions, which may provide a general approach to tune the surface morphology of other transition metal oxide materials. Confirmed by the EIS measurement and DFT calculation, our studies can further suggest the postgrowth treatment method of semiconductor electrodes for enhanced PEC performances.

METHODS

Synthesis, Etching, and Reducing of WO_3 Nanoflakes. WO_3 nanoflakes were synthesized by a modified hydrothermal method. Briefly, a seed solution prepared by dissolving 2.50 g of H_2WO_4 and 1.0 g of poly(vinyl alcohol) (PVA) into 34 mL of H_2O_2 (30 wt %) was spin-coated onto fluorine-doped tin oxide substrates at 2500 rpm, followed by annealing at 500 °C in air for 2 h. Another H_2WO_4 solution was prepared by adding 5.0 g of H_2WO_4 and 68 mL of H_2O_2 (30 wt %) into 100 mL of H_2O and stirred at 95 °C to dissolve. This H_2WO_4 solution was then diluted to 0.05 M for the hydrothermal process. In order to prepare the hydrothermal precursor solution, 3 mL of H_2WO_4 (0.05 M), 0.02 g of oxalic acid, 0.02 g of urea, 12.5 mL of acetonitrile, and 0.5 mL of HCl (6 M) were added into a 50 mL beaker and stirred to clear. An FTO substrate precoated with WO_3 seed was placed into a 25 mL Teflon-lined stainless steel autoclave filled with the as-prepared precursor solution, which was then kept at 180 °C for 2 h. Finally, the obtained sample was annealed at 500 °C in air for 2 h.

A dual etching and reducing solution was prepared by mixing 0.175 g of poly(vinyl pyrrolidone), 0.3 g of ascorbic acid, and 30 mL of H_2O, and then the solution was stirred at 90 °C for 4 h. Afterward, an FTO substrate (grown with WO_3 nanoflakes) was placed into the solution and kept at 90 °C for another 4 h. For the pure etching or pure reducing process, ascorbic acid or PVP was removed from the aforementioned solution, respectively.

Photoelectrochemical Measurement. The PEC measurement was taken in a typical three-electrode quartz cell. The prepared sample was used as the working electrode. A Pt wire and a Ag/AgCl electrode were used as the counter electrode and the reference electrodes, respectively. H_2SO_4 (1 M) was used as the electrolyte. A simulated sunlight coupled with an AM 1.5 G filter (Newport 94022A) was applied. IPCE spectra were collected by a solar simulator (Newport 66902) coupled with a filter (Newport 74010) and an aligned monochromator (Newport 74125). All the electrochemical measurements were carried out by an electrochemical workstation (Autolab PGSTAT 204, Metrohm, Switzerland). The electrochemical impedance spectroscopy was measured with 10 kHz frequency in the dark. The reversible hydrogen potential can be converted from the Ag/AgCl reference electrode potential as $\text{RHE} = V_{vs\ \text{Ag/AgCl}} + E^{\circ}_{\text{Ag/AgCl}} + 0.059 \times \text{pH}$, where $E^{\circ}_{\text{Ag/AgCl}}$ is 0.1976 V at 25 °C. IPCE can be expressed by the equation: $\text{IPCE} = (1240 \times I)/(\lambda \times J_{\text{light}})$, where I is the measured photocurrent density at a specific wavelength, λ is the wavelength of incident light, and J_{light} is the measured irradiance at a specific wavelength. According to the Mott–Schottky equation

$$1/C^2 = 2(E - E_{\text{fb}} - kT/e)/N_{\text{d}}e\varepsilon_0\varepsilon$$

where C is the space charge capacitance in the semiconductor, N_{d} is the charge carrier density, e is the electron charge, ε_0 and ε are the vacuum permittivity and the dielectric constant of the semiconductor, respectively, E is the applied potential, E_{fb} is the flat band potential, T is the temperature, and k is the Boltzmann constant.

Density Functional Theory Calculation. The ion–electron interaction was treated by the projector-augmented wave technique,[38] as implemented in the Vienna ab initio simulation package.[39] The exchange-correlation potential was treated using the Perdew–Burke–Ernzerhof function.[40] The on-site correlation corrections were included using the Hubbard model

(DFT+U approach), and the value of the correlation energy (U) was fixed at 6.2 eV for the 5d orbital of W.[41] The 3D k-mesh was generated by the Monkhorst−Pack scheme, where the density of k-points was determined by lattice constant ($4 \times 4 \times 4$ for the monoclinic phase and $4 \times 4 \times 1$ for the slab model). In the slab model, the vacuum layer was set to be 15 Å between atomic layers. The lattice vectors and atomic positions were optimized according to the guidance of atomic forces, with a criterion of the calculated force on each atom smaller than 0.01 eV/Å. A slab model was built along the (001) surface, as it was easy to be cleaved due to the antiferroelectric distortion along the direction. A $(\sqrt{2} \times \sqrt{2})R45°$ surface, which was found to be the most stable for the reconstructed (001) surface, was built to simulate the system with six layers of WO planes, and the convergence of energy with respect to the number of layers was tested.

Conflict of Interest: The authors declare no competing financial interest.

Acknowledgment. We thank the following funding agencies for supporting this work: the National Key Basic Research Program of China (2013CB934104), the Natural Science Foundation of China (21322311, 21473038, 21071033), the Science and Technology Commission of Shanghai Municipality (14JC1490500), the Doctoral Fund of Ministry of Education of China (20130071110031), the Program for Professor of Special Appointment (Eastern Scholar) at Shanghai Institutions of Higher Learning, and the Deanship of Scientific Research of King Saud University (IHCRG#14-102). W.L., P.D., and X.L. acknowledge the support of Hui-Chun Chin & Tsung-Dao Lee Chinese Undergraduate Research Endowment.

Supporting Information Available: Supporting figures. This material is available free of charge *via* the Internet at http://pubs.acs.org.

REFERENCES AND NOTES

1. Xu, M.; Da, P.; Wu, H.; Zhao, D.; Zheng, G. Controlled Sn-Doping in TiO_2 Nanowire Photoanodes with Enhanced Photoelectrochemical Conversion. *Nano Lett.* **2012**, *12*, 1503–1508.
2. Xia, X.; Luo, J.; Zeng, Z.; Guan, C.; Zhang, Y.; Tu, J.; Zhang, H.; Fan, H. J. Integrated Photoelectrochemical Energy Storage: Solar Hydrogen Generation and Supercapacitor. *Sci. Rep.* **2012**, *2*, 981.
3. Wang, G.; Wang, H.; Ling, Y.; Tang, Y.; Yang, X.; Fitzmorris, R. C.; Wang, C.; Zhang, J. Z.; Li, Y. Hydrogen-Treated TiO_2 Nanowire Arrays for Photoelectrochemical Water Splitting. *Nano Lett.* **2011**, *11*, 3026–3033.
4. Sivula, K.; Le Formal, F.; Grätzel, M. Solar Water Splitting: Progress Using Hematite (α-Fe_2O_3) Photoelectrodes. *ChemSusChem* **2011**, *4*, 432–449.
5. Li, L.; Yu, Y.; Meng, F.; Tan, Y.; Hamers, R. J.; Jin, S. Facile Solution Synthesis of α-$FeF_3 \cdot 3H_2O$ Nanowires and Their Conversion to α-Fe_2O_3 Nanowires for Photoelectrochemical Application. *Nano Lett.* **2012**, *12*, 724–731.
6. Du, C.; Yang, X.; Mayer, M. T.; Hoyt, H.; Xie, J.; McMahon, G.; Bischoping, G.; Wang, D. Hematite-Based Water Splitting with Low Turn-On Voltages. *Angew. Chem., Int. Ed.* **2013**, *52*, 12692–12695.
7. Liu, X.; Wang, F.; Wang, Q. Nanostructure-Based WO_3 Photoanodes for Photoelectrochemical Water Splitting. *Phys. Chem. Chem. Phys.* **2012**, *14*, 7894–7911.
8. Rao, P. M.; Cai, L.; Liu, C.; Cho, I. S.; Lee, C. H.; Weisse, J. M.; Yang, P.; Zheng, X. Simultaneously Efficient Light Absorption and Charge Separation in $WO_3/BiVO_4$ Core/Shell Nanowire Photoanode for Photoelectrochemical Water Oxidation. *Nano Lett.* **2014**, *14*, 1099–1105.
9. Hochbaum, A. I.; Yang, P. Semiconductor Nanowires for Energy Conversion. *Chem. Rev.* **2010**, *110*, 527–546.
10. Walter, M. G.; Warren, E. L.; McKone, J. R.; Boettcher, S. W.; Mi, Q.; Santori, E. A.; Lewis, N. S. Solar Water Splitting Cells. *Chem. Rev.* **2010**, *110*, 6446–6473.
11. Wang, X.; Liow, C.; Qi, D.; Zhu, B.; Leow, W. R.; Wang, H.; Xue, C.; Chen, X.; Li, S. Programmable Photo-electrochemical Hydrogen Evolution Based on Multi-segmented CdS−Au Nanorod Arrays. *Adv. Mater.* **2014**, *26*, 3506–3512.
12. Mi, Q.; Zhanaidarova, A.; Brunschwig, B. S.; Gray, H. B.; Lewis, N. S. A Quantitative Assessment of the Competition between Water and Anion Oxidation at WO_3 Photoanodes in Acidic Aqueous Electrolytes. *Energy Environ. Sci.* **2012**, *5*, 5694–5700.
13. Sun, Y.; Murphy, C. J.; Reyes-Gil, K. R.; Reyes-Garcia, E. A.; Thornton, J. M.; Morris, N. A.; Raftery, D. Photoelectrochemical and Structural Characterization of Carbon-Doped WO Films Prepared *via* Spray Pyrolysis. *Int. J. Hydrogen Energy* **2009**, *34*, 8476–8484.
14. Xi, G.; Yue, B.; Cao, J.; Ye, J. Fe_3O_4/WO_3 Hierarchical Core−Shell Structure: High-Performance and Recyclable Visible-Light Photocatalysis. *Chem.—Eur. J.* **2011**, *17*, 5145–5154.
15. Su, J.; Feng, X.; Sloppy, J. D.; Guo, L.; Grimes, C. A. Vertically Aligned WO_3 Nanowire Arrays Grown Directly on Transparent Conducting Oxide Coated Glass: Synthesis and Photoelectrochemical Properties. *Nano Lett.* **2011**, *11*, 203–208.
16. Amano, F.; Li, D.; Ohtani, B. Fabrication and Photoelectrochemical Property of Tungsten(VI) Oxide Films with a Flake-Wall Structure. *Chem. Commun.* **2010**, *46*, 2769–2771.
17. De Tacconi, N.; Chenthamarakshan, C.; Yogeeswaran, G.; Watcharenwong, A.; De Zoysa, R.; Basit, N.; Rajeshwar, K. Nanoporous TiO_2 and WO_3 Films by Anodization of Titanium and Tungsten Substrates: Influence of Process Variables on Morphology and Photoelectrochemical Response. *J. Phys. Chem. B* **2006**, *110*, 25347–25355.
18. Kim, J. K.; Shin, K.; Cho, S. M.; Lee, T.-W.; Park, J. H. Synthesis of Transparent Mesoporous Tungsten Trioxide Films with Enhanced Photoelectrochemical Response: Application to Unassisted Solar Water Splitting. *Energy Environ. Sci.* **2011**, *4*, 1465–1470.
19. Wang, Y.; Zhang, Y.-Y.; Tang, J.; Wu, H.; Xu, M.; Peng, Z.; Gong, X.-G.; Zheng, G. Simultaneous Etching and Doping of TiO_2 Nanowire Arrays for Enhanced Photoelectrochemical Performance. *ACS Nano* **2013**, *7*, 9375–9383.
20. Pan, J. H.; Wang, X. Z.; Huang, Q.; Shen, C.; Koh, Z. Y.; Wang, Q.; Engel, A.; Bahnemann, D. W. Large-Scale Synthesis of Urchin-like Mesoporous TiO_2 Hollow Spheres by Targeted Etching and Their Photoelectrochemical Properties. *Adv. Funct. Mater.* **2014**, *24*, 95–104.
21. Basilio, A. M.; Hsu, Y.-K.; Tu, W.-H.; Yen, C.-H.; Hsu, G.-M.; Chyan, O.; Chyan, Y.; Hwang, J.-S.; Chen, Y.-T.; Chen, L.-C. Enhancement of the Energy Photoconversion Efficiency through Crystallographic Etching of a c-Plane GaN Thin Film. *J. Mater. Chem.* **2010**, *20*, 8118–8125.
22. Amano, F.; Ebina, T.; Ohtani, B. Enhancement of Photocathodic Stability of p-Type Copper(I) Oxide Electrodes by Surface Etching Treatment. *Thin Solid Films* **2014**, *550*, 340–346.
23. Wang, G.; Ling, Y.; Li, Y. Oxygen-Deficient Metal Oxide Nanostructures for Photoelectrochemical Water Oxidation and Other Applications. *Nanoscale* **2012**, *4*, 6682–6691.
24. Wang, G.; Ling, Y.; Wang, H.; Yang, X.; Wang, C.; Zhang, J. Z.; Li, Y. Hydrogen-Treated WO_3 Nanoflakes Show Enhanced Photostability. *Energy Environ. Sci.* **2012**, *5*, 6180–6187.
25. Wang, H.; Kalytchuk, S.; Yang, H.; He, L.; Hu, C.; Teoh, W. Y.; Rogach, A. L. Hierarchical Growth of SnO_2 Nanostructured Films on FTO Substrates: Structural Defects Induced by Sn(II) Self-Doping and Their Effects on Optical and Photoelectrochemical Properties. *Nanoscale* **2014**, *6*, 6084–6091.
26. Wang, Y.; Tang, J.; Zhou, T.; Da, P.; Li, J.; Kong, B.; Yang, Z.; Zheng, G. Reversible Chemical Tuning of Charge Carriers for Enhanced Photoelectrochemical Conversion and Probing of Living Cells. *Small* **2014**, 10.1002/smll.201401059.
27. Wang, Y.; Zhou, T.; Jiang, K.; Da, P.; Peng, Z.; Tang, J.; Kong, B.; Cai, W. B.; Yang, Z.; Zheng, G. Reduced Mesoporous Co_3O_4 Nanowires as Efficient Water Oxidation Electrocatalysts and Supercapacitor Electrodes. *Adv. Energy Mater.* **2014**, 10.1002/aenm.201400696.
28. Wu, H.; Xu, M.; Da, P.; Li, W.; Jia, D.; Zheng, G. WO_3-Reduced Graphene Oxide Composites with Enhanced Charge

Transfer for Photoelectrochemical Conversion. *Phys. Chem. Chem. Phys.* **2013**, *15*, 16138–16142.

29. Ko, R.-M.; Wang, S.-J.; Tsai, W.-C.; Liou, B.-W.; Lin, Y.-R. The Evolution of Tungsten Oxide Nanostructures from Nanowires to Nanosheets. *CrystEngComm* **2009**, *11*, 1529.
30. Manciu, F. S.; Enriquez, J. L.; Durrer, W. G.; Yun, Y.; Ramana, C. V.; Gullapalli, S. K. Spectroscopic Analysis of Tungsten Oxide Thin Films. *J. Mater. Res.* **2010**, *25*, 2401–2406.
31. Bathe, S. R.; Patil, P. Titanium Doping Effects in Electrochromic Pulsed Spray Pyrolysed WO_3 Thin Films. *Solid State Ionics* **2008**, *179*, 314–323.
32. Moulzolf, S. C.; Ding, S.-a.; Lad, R. J. Stoichiometry and Microstructure Effects on Tungsten Oxide Chemiresistive Films. *Sens. Actuators, B* **2001**, *77*, 375–382.
33. Tauc, J.; Grigorovici, R.; Vancu, A. Optical Properties and Electronic Structure of Amorphous Germanium. *Phys. Status Solidi B* **1966**, *15*, 627–637.
34. Reyes-Gil, K. R.; Wiggenhorn, C.; Brunschwig, B. S.; Lewis, N. S. Comparison between the Quantum Yields of Compact and Porous WO_3 Photoanodes. *J. Phys. Chem. C* **2013**, *117*, 14947–14957.
35. Ye, M.; Gong, J.; Lai, Y.; Lin, C.; Lin, Z. High-Efficiency Photoelectrocatalytic Hydrogen Generation Enabled by Palladium Quantum Dots-Sensitized TiO_2 Nanotube Arrays. *J. Am. Chem. Soc.* **2012**, *134*, 15720–15723.
36. Lambert-Mauriat, C.; Oison, V.; Saadi, L.; Aguir, K. *Ab Initio* Study of Oxygen Point Defects on Tungsten Trioxide Surface. *Surf. Sci.* **2012**, *606*, 40–45.
37. Yin, W.-J.; Tang, H.; Wei, S.-H.; Al-Jassim, M. M.; Turner, J.; Yan, Y. Band Structure Engineering of Semiconductors for Enhanced Photoelectrochemical Water Splitting: The Case of TiO_2. *Phys. Rev. B* **2010**, 82.
38. Blöchl, P. E. Projector Augmented-Wave Method. *Phys. Rev. B* **1994**, *50*, 17953–17979.
39. Kresse, G.; Hafner, J. *Ab Initio* Molecular-Dynamics Simulation of the Liquid-Metal-Amorphous-Semiconductor Transition in Germanium. *Phys. Rev. B* **1994**, *49*, 14251–14269.
40. Perdew, J. P.; Burke, K.; Ernzerhof, M. Generalized Gradient Approximation Made Simple. *Phys. Rev. Lett.* **1996**, *77*, 3865–3868.
41. Wu, Y.; Chan, M. K. Y.; Ceder, G. Prediction of Semiconductor Band Edge Positions in Aqueous Environments from First Principles. *Phys. Rev. B* **2011**, *83*, 235301.